Proceedings of the International Conference on Heat Exchanger Fouling and Cleaning - 2024 (Peer-reviewed)
April 21–26, 2024, Lisbon, Portugal; Editors: H.U. Zettler and E.M. Ishiyama

INVESTIGATION OF FOULING ROUGHNESS INDUCED HEAT TRANSFER IMPROVEMENT USING A STEREOSCOPIC MICRO PIV

***L. Rohwer, A. F. Wasserfuhr, W. Augustin and S. Scholl**
Technische Universität Braunschweig, Institute for Chemical and Thermal Process Engineering, Braunschweig, Germany
*Corresponding author: l.rohwer@tu-braunschweig.de

ABSTRACT

This study examines the relationship between surface roughness caused by crystal fouling layers and heat transfer in a controlled flow environment. Heat exchanger fouling is a persistent challenge in industrial processes that significantly affects efficiency and operational costs. The investigation uses Stereoscopic Micro Particle Image Velocimetry (Stereo µPIV) to explore local micro-scale effects on heat transfer under fouling conditions. Crystal fouling layers, generated from $CaSO_4$ material system, are introduced into a flow channel to simulate realistic fouling conditions. By implementing a fouling layer characterization parameter, the growth phase of the fouling layer can be related to its effects on pressure drop and heat transfer. The study uses advanced visualization techniques to capture three-dimensional velocity fields and turbulent kinetic energy, providing insights into turbulence intensity in the immediate vicinity of a crystal fouling layer. This turbulence increase can be quantified by the *Turbulent Kinetic Energy*. A direct correlation between the crystal layer characterization and its effects on pressure drop and heat transfer can be observed.

INTRODUCTION

Heat exchanger fouling remains a significant challenge in various industrial processes, leading to decreased efficiency and increased costs [1]. Crystallization fouling represents a major fouling mechanism in heat exchangers and typically can be divided into three phases [2]. The induction is divided into two: The initiation phase, in which the fouling starts with nucleation on the surfaces, which is then followed by the roughness-controlled phase, as shown in Figure 1. In this phase the roughness of the crystal fouling layer induces an enhancement of turbulent convective heat transfer, which superimposes the enhanced heat transfer resistance by the fouling layer. This leads to a short time period in which the heat transfer resistance due to fouling is overcompensated by the increased roughness, resulting in an apparent negative thermal fouling resistances [2].

After this, the crystal growth phase is reached in which the fouling-induced heat transfer resistance exceeds the positive effects of the surface roughness and a compact isolating crystal layer is formed [2].

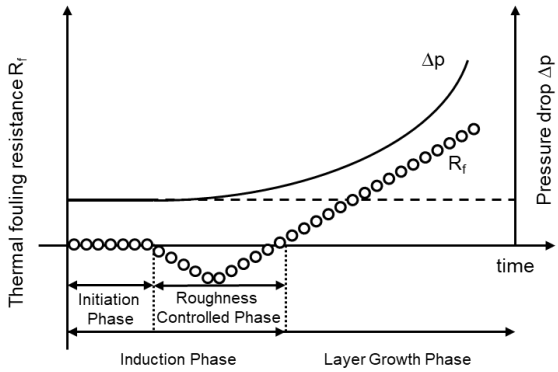

Figure 1: Thermal fouling resistance and pressure drop during different fouling phases (adapted from [2])

The effect of surface roughness on heat transfer has been extensively studied and described. The deliberate modification of surface roughness in heat-transferring equipment is therefore widespread [3]. The effect of surface roughness on heat transfer is determined by the properties of the roughness, whereby the size, orientation and distribution of the roughness-inducing elements are decisive.

Many heat transfer correlations accounting for surface roughness effects have been presented while describing well defined surface geometries [2]. The description of the effect of crystallization fouling on heat transfer, especially due to the large number of crystal layer topographies that can occur in different material systems, is a question that goes beyond this.

This study presents an experimental approach to investigate the local micro scale effects on heat transfer under fouling conditions applying Stereoscopic Micro Particle Image Velocimetry (Stereo µPIV) in a flow channel. The study focuses on understanding the impact of surface roughness induced by crystal fouling layers on local turbulence characteristics within a controlled flow environment. Crystal fouling layers from the material systems $CaSO_4$ are generated, using an independent batch reactor setup. In addition,

ISBN: 978-0-9984188-3-4; Published online www.heatexchanger-fouling.com

additively manufactured (AM) structures are introduced into the flow channel to simulate flow conditions comparable to crystal fouling layers. The AM structures allow a controlled and clearly geometrically defined change in the flow channel geometry, which makes it easy to investigate effects such as the local pressure loss caused by the channel constriction. Additionally, they can be designed to to recreate structures used in previous studies and thus validate the results from the experimental setup used here.

Stereoscopic Micro PIV is used to capture three-dimensional velocity fields in a two-dimensional plane and therefore extend classical PIV measurement systems into the third spatial dimension. Laser-excited tracer particles tracing the streamlines in the flowing fluid are captured and their change in position over time is observed. This technique employs two cameras to create a stereoscopic view, enabling the simultaneous measurement of all three velocity components [4]. To calculate three-dimensional velocity vectors, two images from each camera are required, taken within a time range of a few microseconds. The temporal range of the examined flow velocity in the flow channel determines the synchronization with the time between the laser pulses.

After acquisition, the image pair undergoes digital processing to eliminate noise and inaccurately detected tracers by applying a threshold value. Tracer patterns between two images are identified through transformations, such as the discrete Fourier transform and the discrete cosine transform. The determination of the displacement of each tracer in all three spatial dimensions is facilitated by knowledge of each tracer's location in the first and second images.

The velocity of a tracer (v_i) is calculated as a vector, which incorporates information about the tracers' displacement (s_i), the microscope's magnification, and the time difference (Δt) between the two images. The flow channel's coordinate system uses the x-axis in the flow direction, the y-axis perpendicular to the flow direction, and the z-axis towards the camera. The calculation for the tracer velocity in three dimensions is expressed as follows:

$$\vec{v}_{Tracer} = \begin{pmatrix} v_x \\ v_y \\ v_z \end{pmatrix} \quad (1)$$

In addition to the local velocity vectors the *Turbulent Kinetic Energy* (TKE) can be calculated by the according variances σ_i, as shown in equation 2. The TKE characterizes the pulsation intensity into the flow field [5].

$$TKE = 0.5 * (\sigma_x^2 + \sigma_y^2 + \sigma_z^2) \quad (2)$$

The PIV technology has been utilized multiple times to investigate heat transfer improvements due to increased local turbulences. Previous research presented from Virgilio et al. [6] investigated the effect of dimpled structures on heat transfer in a tubular heat exchanger using a planar and a Stereo PIV. Further investigations on wall structures and their effect on heat transfer have been conducted while utilizing a Stereo PIV. Giordano et al. [7] used a Stereo PIV to investigate the flow field downstream of a finite circular cylinder and by this described the influence on the heat transfer topology and enhancement.

This research aims on investigating the interacting effects of surface roughness, induced by crystallization fouling, and heat transfer. [2] Therefore, local flow velocities, local TKE and the surface structures are observed and are compared with the simultaneously measured pressure drop. This shall effectively link these local effects on heat transfer with the occurring overall pressure drop.

EXPERIMENTAL PROCEDURE

Crystal fouling layer

In the course of this work calcium sulfate ($CaSO_4$) was selected as material system, as it forms very distinct crystal structures and is one of the most common water hardeners. $CaSO_4$ forms monoclinic crystal structures with a long needle-like shape, as shown in Figure 2.

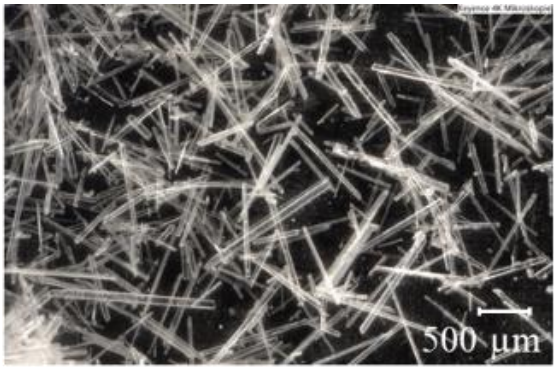

Figure 2: Crystal structure of $CaSO_4$

The crystal fouling layers were produced in a continuously stirred batch reactor, as shown in Figure 3, and subsequently subjected to further external investigations.

ISBN: 978-0-9984188-3-4; Published online www.heatexchanger-fouling.com

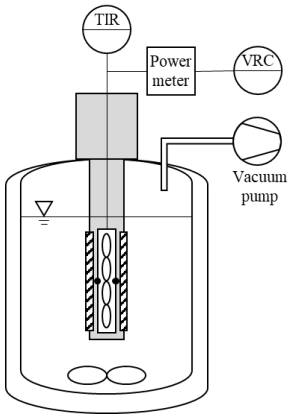

Figure 3: Schematic of the batch fouling apparatus with vacuum pump, adapted from [8]

The reactor can simultaneously hold two sample plates (SP), measuring 80 x 20 x 2 mm, while the continuously stirred aqueous salt solution is tempered. A heating element is located underneath the plates, which allows a constant heat input by means of a power meter.

For the $CaSO_4$ fouling layers used in this work the salt solution, at a concentration of 0.027 mol/L, has been heated to 42°C with a constant heat input of 90 W which resulted in a wall temperature of 60°C. The salt solution was prepared by separately dissolving calcium nitrate tetrahydrate and sodium sulfate in water, which were tempered before being added to the batch reactor.

Preliminary tests with $CaSO_4$ have shown that due to the temperature gradient near the sample plates surface gas bubbles formed. These led to unwanted structural changes in the crystalline deposits. Therefore, a vacuum pump was installed and for all $CaSO_4$ structures the solution was degassed at an absolute pressure of 80 mbar and a temperature of 42 °C for at least 5 minutes. This procedure prevented the occurrence of bubbles on the sample surface and thus avoided the disruption of the crystal structures.

The growth time within the batch reactor was varied between 4 h and 24 h for $CaSO_4$ in order to investigate the fouling layers at different growth states and layer heights.

AM layer design

Additive Manufacturing is a layer-based production technology which allows the production of complex geometries in a single manufacturing step. The technology enables local manufacturing at relatively low costs and efforts while being highly customizable [9]. Due to these advantages, additive manufacturing is suitable for the flexible and short-term production of reference structures, which were used in the context of this work.

Utilizing open market Fuse Deposition Modeling (FDM) printers from *Ultimaker B.V.* (*Ultimaker 2+ Extended*) and *Prusa Research a. s.* (*Prusa MK4)* different reference structures were manufactured from Polylactide polymers. The layer height was set to 200 µm with solid material (infill ratio of 100 %). A nozzle diameter of 0.4 mm was used along all reference structures, resulting in a top surface with a mean arithmetic height of $S_a \approx 20$ µm and maximum height of $S_z \approx 95$ µm. Figure 4 shows the rendering an a microscopic image of one additively manufactured reference structure.

The reference structures have the advantage that they are inert to the fluid and will therefore withstand almost unlimited times inside the flow channel. Therefore, they are very well suited for calibration and method development as long as their properties are comparable to the final crystal structures.

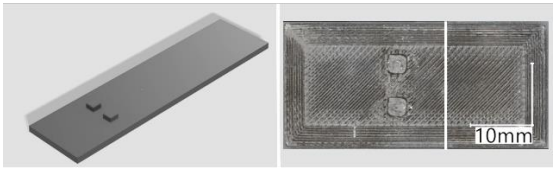

Figure 4: Additively manufactured reference structure (SP12) with 3 x 3 x 1 mm cuboid on a flat surface. Rendering model (left) and microscopic image (right)

Layer characterization

After the production of the crystal fouling layers inside the batch reactor, the fouling layers are characterized. A digital 4 k microscope *Keyence VHX-7000* is used to document the overall view of the fouled test plate, the local layer height and the surface coverage, see Figure 5.

The images were recorded with a 50 x magnification as an assembly of multiple single images and a depth correlation utilizing the depth of field was conducted. A polarization filter limits the reflection effects of the crystal structures.

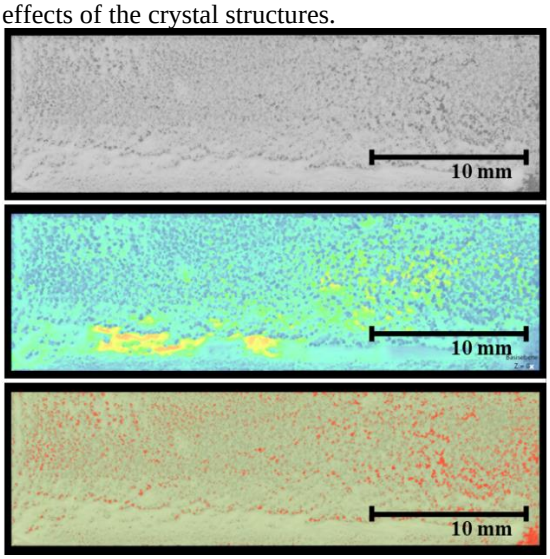

Figure 5: Layer characterization of a $CaSO_4$ crystal layer (SP1) utilizing a digital microscope. Overall image of the fouled test plate (top), layer height analysis (middle) and surface coverage (bottom)

ISBN: 978-0-9984188-3-4; Published online www.heatexchanger-fouling.com

The layer height analysis enables an accurate prediction of the expected maximum and average layer height of the structures subsequently transferred to the PIV channel. The given example in Figure 5 shows that at the bottom section of the plate a significant local increase in layer height can be observed. The surface coverage was also visually analyzed by distinguishing between the different brightness values for the very reflecting crystal structures and the less reflecting steel surface. It should be mentioned that the reflection components in the direction of the microscope lens that are not removed by the polarization filter determine the optical image and not the actual whole reflection of the surface. Due to the more non-directional reflection of the crystals, they still appear brighter than the more directional reflections from the steel surface.

Based on the layer height measurements of the whole sample plate, an integral fouling layer volume over the whole plate can be estimated. Next to this a gravimetric analysis allows to approximate the mean density of the fouling layer. Therefore, the sample plate is weighed before being placed in the batch reactor. After the crystal growth the sample plate with fouling layer is given a brief rinse with water and dried in a drying cabinet after and weighted again, giving the overall mass of the fouling layer on the sample plate.

To further evaluate the structure of the crystal fouling layers the arithmetical mean height of the surface S_a and the maximum height of the surface S_z were used. Those parameters are extensions of the known surface roughness parameters, which refer to the roughness along a line on a plane, and therefore refer to the whole investigated plane. S_a is defined as the sum of difference in height of each point compared to the arithmetic mean of the surface divided by the observed surface area, as shown in equation 3 [10].

$$S_a = \frac{1}{A}\iint_A |Z(x,y)|\ dxdy \qquad (3)$$

Whereas S_z is defined as the sum of the absolute values of the height value of the highest peak and the height value of the lowest indentation within the defined range, as shown in equation 4.

$$S_z = S_{peak} + S_{indent} \qquad (4)$$

Experimental setup of the Stereo µPIV

The experiments were conducted in a flow channel consisting of a housing and a lid with windows for optical accessibility, as shown in Figure 6 and described in Kasper et al. [11]. The measuring section of the channel accommodates artificially manufactured test plates with varying surface structures and crystal fouling layers as described above. The cross-section of the flow channel is rectangular, measuring 18 × 4 mm over a length of 520 mm. The flow profile is fully developed along the inlet zone, which is located 350 mm upstream of the measuring section. The flow velocity can be adjusted within the range of 1 m/s to 4 m/s, resulting in Reynolds numbers ranging from Re = 8,200 to 32,700 in an empty channel. A mounting for inserting 20 x 80 mm sample plates was implemented inside the flow channel.

The flow channel is equipped with a differential pressure sensor (OMEGA PD23-V-0.5) which can measure the pressure drop over the whole length of the flow channel over time in a range from 0-500 mbar and an accuracy of 0.5 mbar. Additionally, the temperature of the entering and exiting salt solution are recorded with type K thermocouples which are specified with a measurement accuracy of 0.5 °C. To investigate the effect on heat transfer the bottom of the flow channel with the sample plates located may be heated by heating water. As described by Deponte et al. [12], this allows for thermal balancing and thus heat transfer assessment.

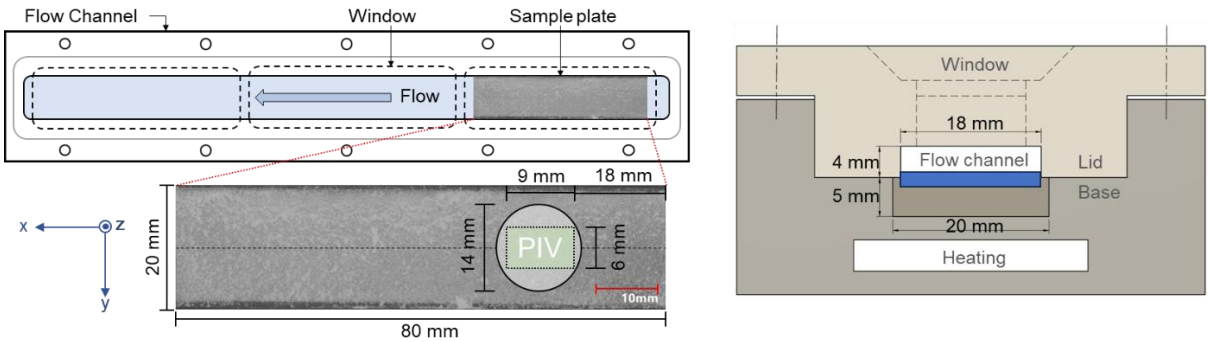

Figure 6: Schematic visualization of the flow channel and sample plate position

ISBN: 978-0-9984188-3-4; Published online www.heatexchanger-fouling.com

A high-resolution 2D-3C Stereo Micro PIV system, which consists of a high repetition-rate laser source, two high-speed cameras, and data acquisition system was used to measure the flow. The flow was seeded with 10 µm water-insoluble PMMA plastic spheres which are fluorescent due to their doping with rhodamine B. Those tracer particles were excited by a double pulsed high-speed Nd:YAG laser that emits green light at $\lambda = 532$ nm and at 10 mJ/pulse. The laser light enters the system through a liquid light guide.

Two 8-bit high speed HiSense Zyla USB scientific complementary metal oxide semiconductor (sCMOS) cameras with 40 Hz frame rate at a full resolution of 2560 x 2160 pixel were used to capture the images. The pixel pitch of the cameras was 3 µm. The images were acquired at a frame rate of 10 Hz. The field of view (FOV) of the camera was set to approximately 14 mm in diameter, as shown in Figure 6. The Stereo µPIV setup is positioned above the flow channel to visually access the flow channel through the windows above.

After adjusting the settings and before taking any measurements, a stereoscopic calibration of the cameras aligns and rectifies the images captured by both cameras. This calibration uses a model of the flow channel. The model includes two micrometer screws that allow for vertical movement of the target on a metal plate. A glass plate with the same thickness as the lid of the flow channel is positioned above the target. The model housing was filled with water to a depth comparable to that of the flow channel, and a specific distance of 4 mm was established between the target surface and the glass plate. For calibration, the microscope's focus was adjusted to align with the target, and a single image per camera was saved. The target was positioned at various heights using the micrometer screws, and additional images were captured at each position after adjusting the microscope focus. The position of the target relative to the original 4 mm position was defined and calibrated for each image using the divergent position of the microscope.

After the acquisition of an image assembly the captured images underwent an image processing procedure to enhance their quality. Initially, the background was subtracted by applying a mean value filter to the image pair. The resulting image was then subtracted from the single frame to mitigate continuous noise emanating from the background. This process aimed to isolate the fluorescent signal emitted by the tracer particles, which were in motion during the time between pulses.

Subsequently, the images were subjected to analysis utilizing an adaptive correlation method. This approach iteratively adjusted the shape and size of interrogation areas based on flow gradients and light intensities. In regions with substantial information, small interrogation areas were employed, while large interrogation areas were utilized in regions with limited information. The initial size of the interrogation grid was configured to 64x64, incorporating a horizontal and vertical overlap of 50%.

In cases where multiple image pairs were captured, which is recommended for achieving gapless images, a merged image could be generated from the calculated vectors of the individual images [13].

RESULTS AND DISCUSSION

Validation

To validate the differential pressure measurement and the mean flow velocity measurement utilizing the Stereo µPIV, an experimental validation series was conducted. Constricting sample plates were produced in stages using additive manufacturing. These constrictions correspond to a sample plate with a homogeneous crystal layer heights of 0 mm to 3 mm in 0.5 mm increments. Figure 7 shows the results of this validation process.

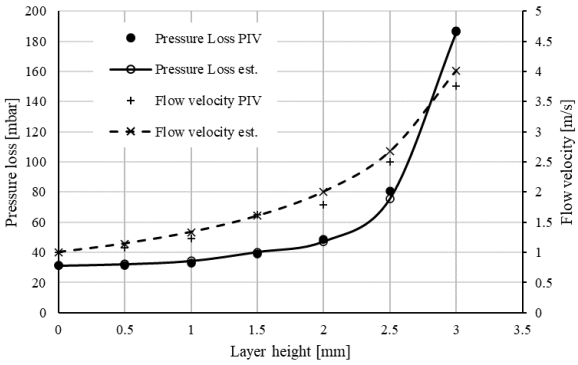

Figure 7: Pressure drop and flow velocity over layer height of artificial structure in rectangular flow channel

It is evident that the measured and the estimated pressure drop follow the same course. The pressure drop was calculated based on the pressure drop of the empty flow channel, taking into account the step caused by the layer height of the sample plate and the local change in flow velocity. To evaluate the effect of the sudden narrowing of the flow channel due to the sample plate, a pressure drop coefficient ξ was calculated for each layer height following equation 5 [14].

$$\xi = 0.5 * \left(1 - \frac{A_2}{A_1}\right) \qquad (5)$$

A_1 corresponds to the cross-sectional area before the narrowing by the layer and A_2 corresponds to the cross-sectional area during the narrowing by the layer. Resulting from this the pressure drop for the flow channel narrowing was estimated by the following equation [14].

ISBN: 978-0-9984188-3-4; Published online www.heatexchanger-fouling.com

$$\Delta p_{step} = \frac{\xi * \rho * v^2}{2} \quad (6)$$

Furthermore, the pressure drop inside the narrowed rectangular flow channel section was estimated. For this a friction factor λ was taken from the moody chart according to the corresponding Reynolds number. The pressure drop for the narrowed section was calculated following equation 7 [14].

$$\Delta p_{nar} = \lambda * \frac{L}{d_H} * \frac{\rho * v^2}{2} \quad (7)$$

The total estimated pressure drop then was calculated as the sum of these three.

$$\Delta p_{est} = \Delta p_0 + \Delta p_{nar} + \Delta p_{step} \quad (8)$$

At layer heights up to 2 mm the deviation between the estimated and the measured pressure drop are between 1 % to 3 %. For 2.5 mm and 3 mm layer heights the measured differential pressure exceeds the estimated differential pressure by up to 6 %, with a standard deviation of less than 0.5 % for the measured pressure drop, which was determined as an average value over a 5-minute measurement.
The flow velocity was measured by focusing the Stereo µPIV in the main flow in the middle of the free cross section of the flow channel with a depth of field of 50 µm. After this the flow velocity was evaluated as the mean value of all recorded velocity vectors in the measuring range. Again, the comparison between calculated velocity values and the measured velocities shows a very good fit. Only at higher flow velocities and higher artificial structures the measured mean flow velocity is lower with a deviation of up to 11 %. This effect might be caused by an inaccuracy in the focal plane placement in the flow channel. If the recorded velocity vectors are too close to the channel walls a slight decrease in flow velocity is expected, due to the laminar boundary layer.
In conclusion, it can be stated that the pressure drop measurement and flow velocity determination could thus be validated.

Layer characterization

The layer characterization was conducted for the $CaSO_4$ fouling structures. Additionally, plain steel plates were characterized as reference.

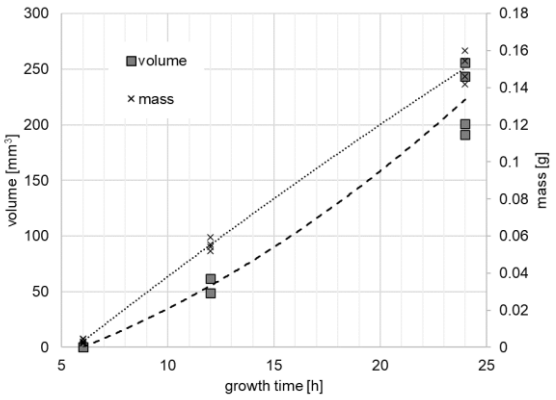

Figure 8: Fouling mass and fouling volume on a sample plate over growth time in batch apparatus

Figure 8 shows the accumulated fouling mass and fouling volume for different growth times. It is clearly evident that both fouling mass and fouling volume continuously increase within the time period of 24h. This indicates that the general salt concentration within the bulk remains constant due to crystal formation to such an extent that the driving force of crystallization, the local supersaturation near the sample plate wall, does not noticeably decrease.

In comparison, a clearly asymptotic trend can be recognized for the surface coverage over time, shown in Figure 9. After approximately 12 hours, the surface coverage reaches over 80 % and then rises with a significantly lower gradient to 91 % after 24 hours. The deviation between the different measurements for the surface coverage is hereby in the tenths of a percent range.

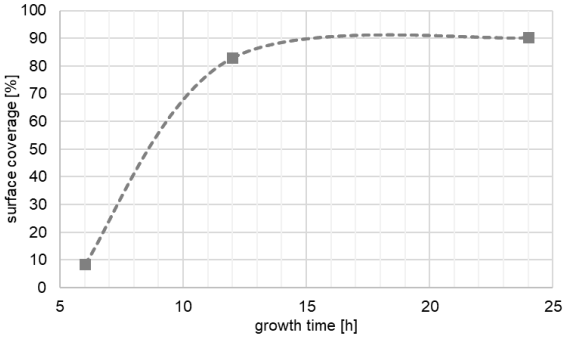

Figure 9: Surface coverage of the fouling layer on the sample plate over growth time in batch apparatus

When looking at the mean arithmetic height and the maximum height, it is noticeable that there is also a change in trend over the growth period. Figure 10 shows that the mean arithmetic height increases significantly between the 6 h and the 12 h sample plates but increases less intensely between the 12 h and 24 h. The maximum height follows a similar trend but reaches much higher roughness values.

ISBN: 978-0-9984188-3-4; Published online www.heatexchanger-fouling.com

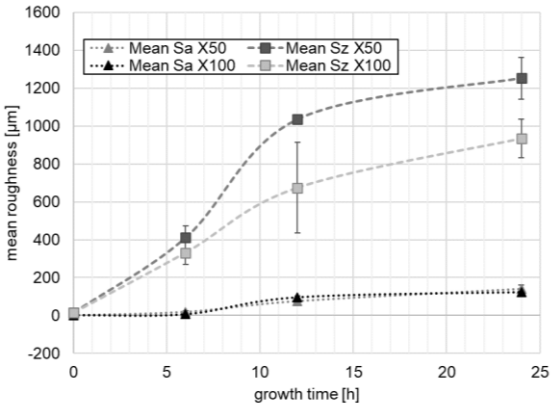

Figure 10: Maximum height S_z and mean arithmetic height S_a over growing time in batch apparatus

This corresponds to expectations, as the monoclinic crystal structures with a long needle-like shape of the $CaSO_4$ crystal layers can reach high maximum values, depending on the spatial position of individual crystal tips, with a lower average height on the surface.

In conjunction with the classification of the crystallization fouling into different phases according to Schlüter et al. [15], a clear differentiation can be made here based on the increase in mass and volume, the surface coverage and the increase in roughness. It can be seen that the induction phase has already been overcome after 6 hours, but only a few crystals have grown on the sample plate. After 12 and 24 hours, however, a covering crystal layer has formed. The total mass on the plate continues to increase, whereby the surface coverage and roughness increase less rapidly. According to Schlüter et al.`s model, it can therefore be assumed that growth occurs on existing layers, resulting in the formation of more compact sub-layers with a less variable roughness of the top layers.

Crystal layer morphology

The fouling layer characterization suggests that a continuous growth on the sample plates can be observed but the dynamics of roughness increase in comparison to fouling volume and mass are changing. Figure 11 shows the measured pressure drop over the whole flow channel during the pump start-up till constant flow conditions. It is evident that an increasing growth time leads to an increased pressure drop while the pressure drop measured at 6 h growth time does not differ significantly from the clean reference sample plate.

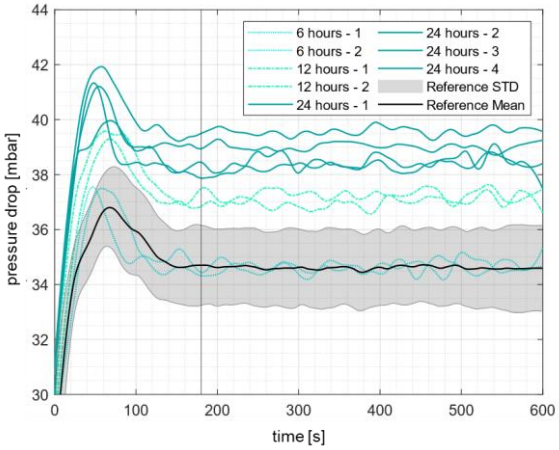

Figure 11: Measured pressure drop over flow channel with different crystal fouling layer growth times and clean reference sample plate

The pressure drop measurement together with the theoretical background from the pressure drop calculation for validation suggests that, the pressure drop is mainly driven by a combination of roughness induced and constricting effects. Combined with the observation of a compact sublayer and significantly slower increase in the roughness formed on it, it is to be expected that different areas of dominant effects can be identified in the comparison of pressure drop and roughness.

Figure 12 shows the pressure drop over the mean arithmetic height S_a and highlights the different growth times of the fouling layer on the sample plates. Comparing the gradient between 6 h and 12 h growth time, in which the roughness controlled phase is present, with the gradient between 12 h and 24 h growth time, in which the growth phase is present, the expected distinction between the dominant pressure drop effects, roughness and constriction, cannot be observed.

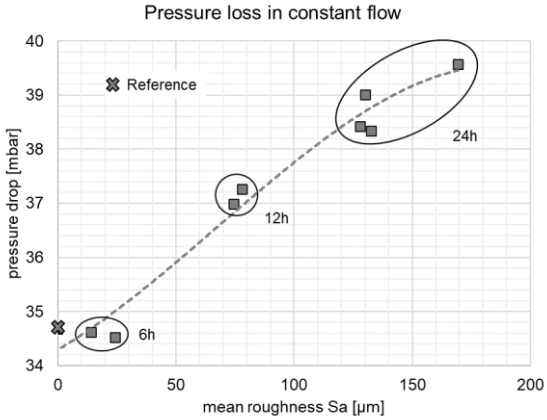

Figure 12: Pressure drop in constant flow over mean roughness S_a after different growth times

This observation suggests that the mean arithmetic height S_a alone is not suitable to describe the crystal layer morphology correctly. Therefore, a roughness parameter S* is introduced, as shown in Figure 13. S* can be divided dependent on the three

ISBN: 978-0-9984188-3-4; Published online www.heatexchanger-fouling.com

depicted fouling phases while the introduction of a maximum height threshold $S_{z,\infty}$ for a fully covered surface allows a better distinction between dominant effects on pressure drop. The maximum height threshold $S_{z,\infty}$ describes the maximum measured height S_z in the limiting case of the fully developed crystal layer without a sublayer.

First crystal structures forming

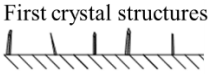

$$S^* = S_a$$

Fully developed crystal layer without a sublayer

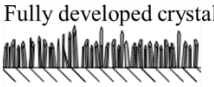

$$S^* = S_a + \underbrace{\left(S_z - S_{z,\infty}\right)}_{0}$$

Fully developed crystal layer with a sublayer

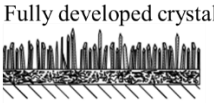

$$S^* = S_a + \left(S_z - S_{z,\infty}\right)$$

Figure 13: Introduction of roughness parameter S*

After the induction phase first crystal structures are forming. During this state the mean arithmetic height describes the fouling layer surface sufficiently, as it can capture all changes in the surface morphology caused by the crystals forming. The maximum height threshold is defined as the maximum height measured at the moment of a fully covered surface without the development of a sublayer. Therefore, in this moment the correcting term equals 0. With further growth from this point, a sublayer is developing. Due to the compact sublayer the base plane for the mean arithmetic height measurement changes from the sample plate surface to the compact sublayers surface. As a result, the mean arithmetic height no longer reflects the growth of the sublayer. In the meantime, however, the measured maximum height S_z continues to increase by the thickness of the sublayer, as this can still be related to the surface of the sample plate at its edge. This leads to a positive correction term as presented in Figure 13 for a fully developed crystal layer including a sublayer underneath.

Implementing this roughness parameter S* and visualizing the pressure drop depending on it, it is clearly evident that the two dominant effects on the pressure drop, roughness and constriction, can now be distinguished, as shown in Figure 14.

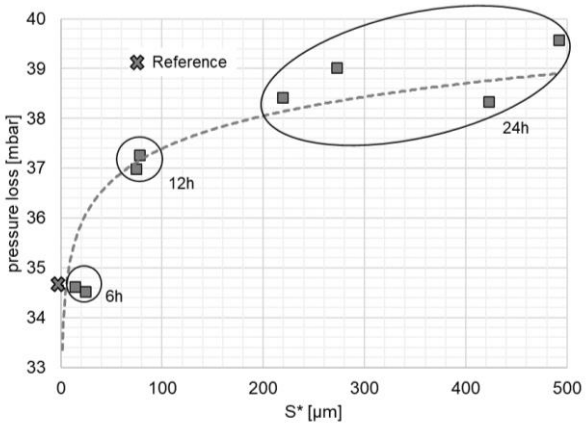

Figure 14: Pressure drop in constant flow over roughness parameter S* after different growth times

Here the maximum height threshold was set to the maximum height measured after a growth time of 12 h. The pressure drop increases with a high gradient between the 6 h and the 12 h growth time crystal layers, while the increase between the 12 h and 24 h crystal layers increases with a much lower gradient. This, together with the before shown characterization of the crystal layer, leads to the conclusion that the different fouling phases can be observed by the introduced methodology.

Flow regime measurement along AM structures

Extending the validation of differential pressure and flow velocity measurements, the additively manufactured sample structures, as shown in Figure 4, can also be used to validate the Stereo µPIV measurements. Those include the three-dimensional fluid dynamics in a two-dimensional measurement plane (2D3C) and the local *Turbulent Kinetic Energy* (TKE).

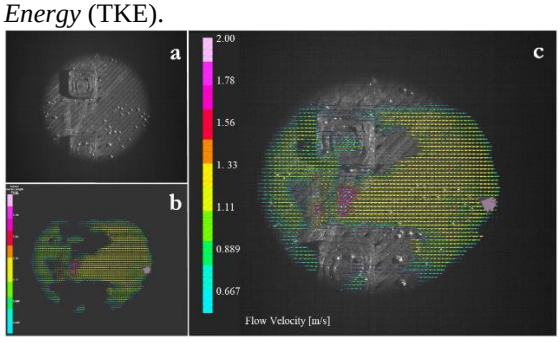

Figure 15: 2D3C measurement over an AM structure with 3 x 3 x 1 mm cuboids (SP12) at a mean flow velocity of 1.10 m/s. Microscope Image (a), 2D3C image (b) and combination (c)

Figure 15 shows the 2D3C measurement of the flow along an AM structure with two 3 x 3 x 1 mm cuboids at a mean flow velocity of 1.10 m/s. The focal plane was located 1 mm above the bottom of the flow channel. The mean flow velocity is calculated and verified by preliminary tests, based on the specified volumetric flow of 260 L/h and the diameter tapered by the cuboid structure.

ISBN: 978-0-9984188-3-4; Published online www.heatexchanger-fouling.com

It is evident, that the Stereo µPIV can identify the location of both cuboids by indicating an area of very little to no velocity vectors. The middle section between both cuboids shows relatively high local flow velocities. Due to an unwanted optical distortion effect at the right edge region of the circular PIV measurement area, caused by a temporary pollution on the cover glass, an incorrect measurement occurred which indicates to high local flow velocities. Therefore, the large local flow velocity vectors on the right edge of Figure 15c and high local TKE in Figure 16 in the same area can be neglected.

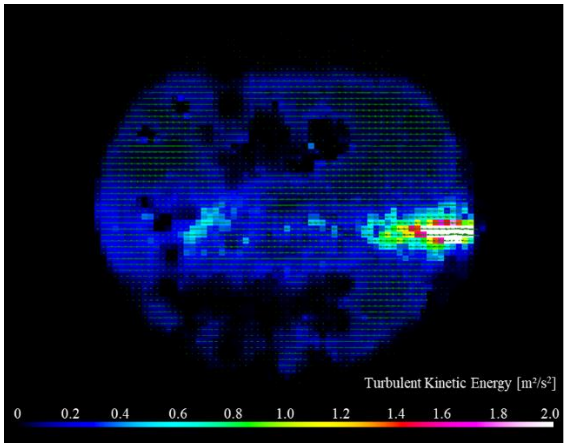

Figure 16: Turbulent Kinetic Energy (TKE) of the additively manufactured sample plate (SP12)

Figure 16 visualizes the local TKE which is computed from the sum of variances scaled by the factor 0.5 as shown in Eq. (3).

The TKE supports the findings derived from the velocity vector image in Figure 15. Especially in the transition zones between areas of higher to lower flow velocity or near the tapering of the cross section between both cuboids, the TKE is increased. Therefore, higher variances in the flow regime can be observed. Again, the temporary cover glass pollution effected the TKE on the right image edge.

Stereo µPIV measurements of crystal structures

The externally grown crystal structures from $CaSO_4$ could successfully be transferred into the Stereo µPIVs flow channel. Furthermore, flow regime measurements could be conducted.

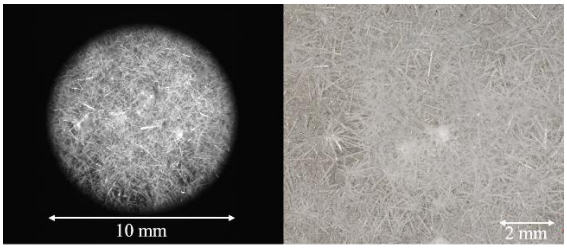

Figure 17: Microscope image of $CaSO_4$ crystal structure (SP1) through the Stereo µPIV setup (left) and Digital Microscope at 20 x magnification (right)

Figure 17 shows the microscope image of a $CaSO_4$ crystal structure through the Stereo µPIV setup on the left and Digital Microscope at 20 x magnification on the right.

The flow velocity vector measurement and the resulting TKE measurement is presented in Figure 18 for a clean reference sample plate on the top and a sample plate with a fouling layer after 24 h growth time. The local flow velocities for the clean reference sample plates suggest a slightly higher local flow velocity. This is due to the fact that the bulk flow rate of 1 m/s (Re = 8200) is regulated by means of a flow measurement. Due to prevailing edge effects, a velocity profile is formed which has slightly increased velocities towards the center of the flow channel and lower flow velocities near the wall.

The comparison between the reference and the 24 h sample plate clearly shows a local flow velocity increase in the red area of the vector map over the crystal structures. Together with the TKE measurement it is clearly evident that the crystal fouling layer is inducing local higher flow velocities and local turbulences into the fluid flow.

ISBN: 978-0-9984188-3-4; Published online www.heatexchanger-fouling.com

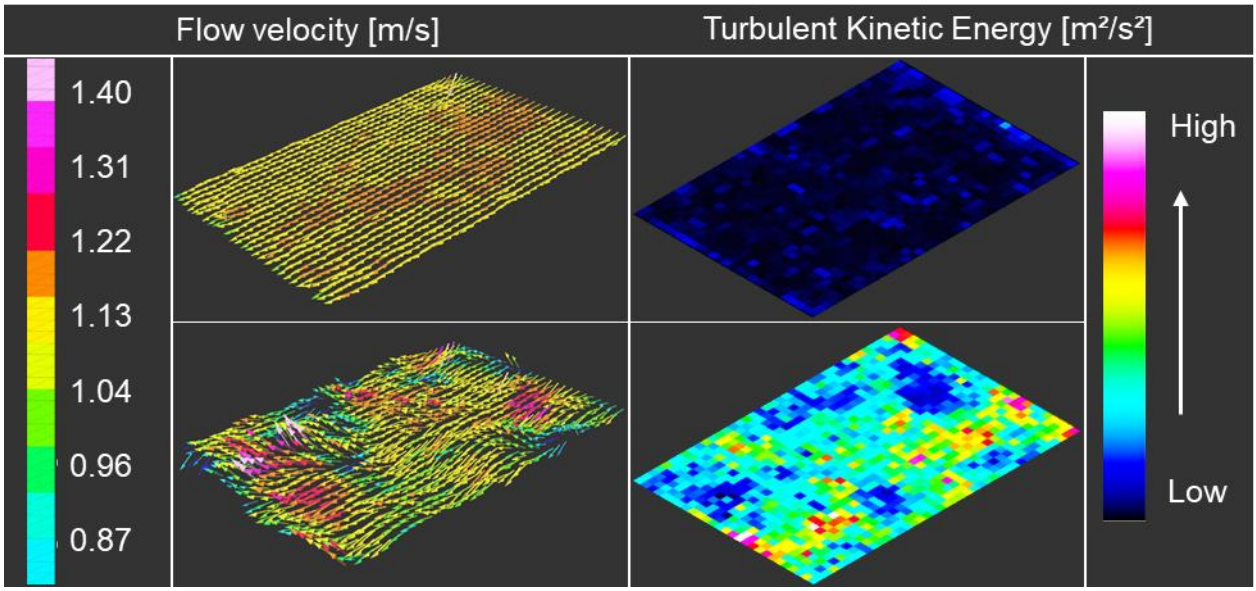

Figure 18: Flow velocity and TKE measurements with the Stereo µPIV at a bulk flow velocity of 1 m/s (Re=8200) with a flow direction from top right to bottom left for a clean reference sample plate (top) and a 24 h fouling sample plate (bottom)

By evaluating the TKE over the whole measurement area and evaluating a mean TKE it is possible to quantify the general effect of the crystal fouling layer on turbulence. Figure 19 presents the mean TKE over thermal fouling resistance for the different growth times. It is evident that a higher turbulence leads to a more negative thermal fouling resistance. This indicates that the longer growth time can leads to higher turbulence inside the fluid flow and therefore improves heat transfer.

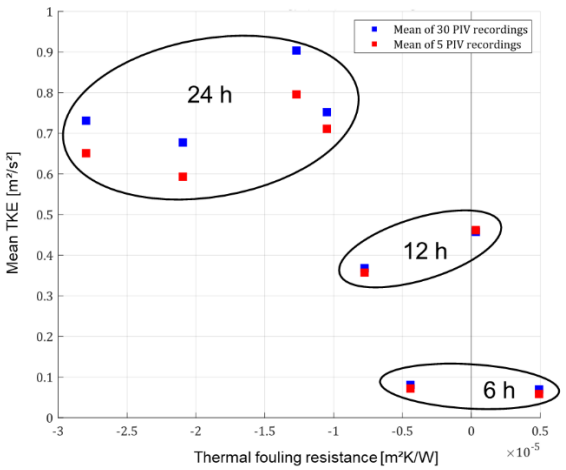

Figure 19: Mean Turbulent Kinetic Energy (TKE) over thermal fouling resistance for different growth times

By connecting those findings with the theoretical thermal fouling resistance trends, as shown in Figure 1, it can be suggested that the crystal fouling layer after a growth time of 24 h, still resembles a structure in the roughness controlled phase. This leads to the assumption that higher growth times will eventually lead to a superimposition of the roughness effects due to the increasing thermal resistance of the growing fouling layer. Figure 20 shows this trend while combining the measurements of the presented crystal fouling layers with additively manufactured reference structures to resemble potential longer growth times.

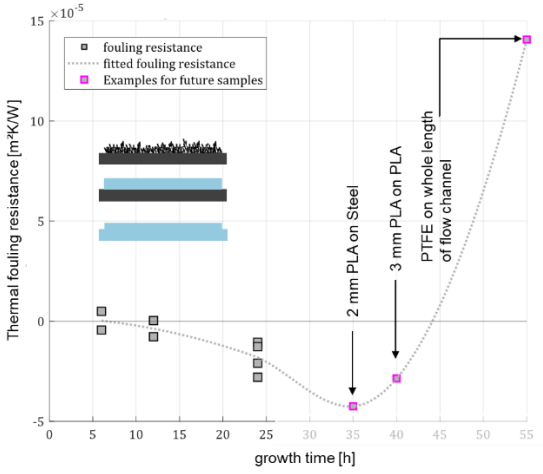

Figure 20: Thermal fouling resistance over growth time with additively manufactured reference structures to resemble potential longer growth times.

By combining different thicknesses of additively manufactured PLA layers (polylactic acid) on top of a clean sample plate, a further decrease in thermal fouling resistance can be observed. A sample plate entirely made from PTFE measured a significant increase in thermal fouling resistance which indicates a decreased heat transfer. This inclusion of reference structures enables a preview of the subsequent investigations of fouling layers with longer growth periods. However, it should be noted that the temporal classification of

ISBN: 978-0-9984188-3-4; Published online www.heatexchanger-fouling.com

the measurement results of all additively manufactured reference structures was chosen based on the expected fouling curve. The growth time is not valid in relation to these measured values after 24 h growth time.

CONCLUSIONS

In the presented study the effects of surface roughness induced by crystal fouling layers have been investigated. First measurements utilizing a Stereo µPIV indicated the increased turbulence near the fouling layer surface. The *Turbulent Kinetic Energy* (TKE) was used to quantify the overall turbulence intensity in the interrogation area. Furthermore, numerous suitable parameters for crystal fouling layer characterization have been utilized and their survey was carried out on individual samples.

To characterize the effect of the crystal topography one material system has been investigated. By growing $CaSO_4$ layers on sample plates inside a batch fouling reactor and transferring them into a Stereo µPIV flow channel, the otherwise difficult to access surfaces were made optically accessible. Furthermore, the easy handling of the crystal layers on the individual sample plates facilitated further analysis.

Due to the TKE increase over growth time and the observed increase in pressure drop it can be concluded that the present crystal layers demonstrably increase the local turbulence. Therefore, a significant influence on the local heat transfer is observed. This effect is countered by the deterioration in heat transfer due to the increase in thermal resistance caused by the crystal layer. To further evaluate this effect, the fouling layer growth time needs to be extended. In addition, it could be considered to compare the effects on the pressure drop to the heat transfer improvement in order to quantify the thermohydraulic disadvantages of the increased turbulence.

Furthermore, by introducing the roughness parameter S* a better description of fouling layer characteristics was introduced.

In the ongoing research, further interests will be addressed. The characterization parameter will be further developed in order to include other properties of the crystal layer morphology in the considerations. Promising approaches for the consideration of porosity, kurtosis and skewness, for example, can be incorporated. Additional measurement series with longer growth times will be conducted.

To ensure a continuous measurement of the fouling layer effects, experimental runs with controlled crystal fouling layer growth in the flow channel will follow. Furthermore, their effects on heat transfer need to be evaluated. The experimental setup already meets the necessary conditions and is currently undergoing further reference measurements.

The proposed study contributes to a deeper understanding of heat transfer in the presence of fouling layers. The combination of advanced visualization techniques and controlled experimental conditions serves as tool to improve the understanding of crystal fouling. The experimental data presented in connection with future work will allow for extending the holistic modelling concept of Schlüter et al. [16]

NOMENCLATURE

A	Area, m²
d_H	Hydraulic diameter, m
L	Length, m
Δp	Pressure drop, mbar
s	Distance, m
S_a	Arithmetical mean height of the surface, µm
S_z	Maximum height of the surface, µm
S^*	Roughness parameter, µm
$S_{z,\infty}$	Maximum height threshold, µm
t	Time, s
T	Temperature, °C
TKE	Turbulent Kinetic Energy, m²/s²
v	Flow velocity, m/s
ρ	Density, kg/m³
λ	Friction Factor, -
σ	Variance, -
ξ	Pressure drop coefficient, -

Subscript

est	*estimated*
i	index
indent	lowest point inside the measurement plane
nar	narrowing in flow channel
peak	highest point inside the measurement plane
step	step in flow channel
x	x-Dimension
y	y-Dimension
z	z-Dimension

REFERENCES

[1] Bott T. R, *Fouling of heat exchangers*. Chemical engineering monographs, vol. 26, Elsevier, Amsterdam, New York, 1995.

[2] Albert F., Augustin W., Scholl S., *Roughness and constriction effects on heat transfer in crystallization fouling*, Chemical Engineering Science, 66:499–509, 2011.

[3] Burck E., *Der Einfluss der Prandtzahl auf den Wärmeübergang und Druckverlust künstlich aufgerauter Strömungskanäle*, Wärme-Stoffübertragung, 1969:87–98, 1969.

[4] Lindken R., Westerweel J., Wieneke B., *Stereoscopic micro particle image velocimetry*, Experiments in Fluids, 41:161–171, 2006.

[5] Li H., Li X., Zhan J., Chen, W., Zong, W., *Study of Turbulent Kinetic Energy and*

ISBN: 978-0-9984188-3-4; Published online www.heatexchanger-fouling.com

Dissipation Based on Fractal Impeller, Sustainability, 15:7772, 2023.
[6] Virgilio M., Dedeyne J. N, van Geem K. M., Marin, G. B., Arts, T., *Dimples in turbulent pipe flows: experimental aero-thermal investigation,* International Journal of Heat and Mass Transfer, 157:119925, 2020.
[7] Giordano R., Ianiro A., Astarita T., Carlomagno, G. M., *Flow field and heat transfer on the base surface of a finite circular cylinder in crossflow*, Applied Thermal Engineering, 49:79–88, 2012.
[8] Tsai J.-H., Cuckston G., Schnöing L., Augustin, W., Scholl, S., Hallmark, B., Wilson, I., *Fluid Dynamic Gauging for Studying Early Stages of Swelling of Fouling Deposits*, Heat Transfer Engineering, 43:1378–1386, 2022.
[9] Öberg C., *Additive Manufacturing Technology*, In: Aldag RJ (ed), Oxford research encyclopedias, Oxford University Press, Oxford, 2016.
[10] Persson B. NJ, *On the Use of Surface Roughness Parameters*, Tribol Lett 71, 2023.
[11] Kasper R., Deponte H., Michel A., Turnow, J., Augustin, W., Scholl, S., Kornev, N., *Numerical investigation of the interaction between local flow structures and particulate fouling on structured heat transfer surfaces*, International Journal of Heat and Fluid Flow, 71:68–79, 2018.
[12] Deponte H., Djendar D., Eckert T., Aloui, F., Augustin, W., Scholl, S., *Fluid dynamic investigation of particle-laden suspensions on dimpled surfaces under fouling conditions*, International Journal of Multiphase Flow, 140:103651, 2021.
[13] Raffel M., Willert C. E, Scarano F., Kähler, C. J., Wereley, S., Kompenhans, J., *Particle Image Velocimetry*, Springer International Publishing, Cham, 2018. (book)
[14] Bohl, W., *Technische Strömungslehre: Stoffeigenschaften von Flüssigkeiten und Gasen, Hydrostatik, Aerostatik, inkompressible Strömungen, kompressible Strömungen, Strömungsmesstechnik*, Vogel-Fachbuch, Vogel, Würzburg, 2002.
[15] Schlüter F., Augustin W., Scholl S., *Modeling local fouling resistances*, Heat Exchanger Fouling and Cleaning, 2019.
[16] Schlüter F., Augustin W., Scholl S., *Introducing a holistic approach to model and link fouling resistances*, Heat Mass Transfer, 57:999–1009, 2021.

ISBN: 978-0-9984188-3-4; Published online www.heatexchanger-fouling.com